

# STAR FORMATION IN THE HIGH-EXTINCTION PLANCK COLD CLUMP PGCC G120.69+2.66

ANLAUG AMANDA DJUPVIK

Nordic Optical Telescope, Rambla José Ana Fernández Pérez 7, ES-38711 Breña Baja, Spain and  
Department of Physics and Astronomy, Aarhus University, Munkegade 120, DK-8000 Aarhus C, Denmark

JOÃO L. YUN

Instituto de Astrofísica e Ciências do Espaço (IA), Universidade de Lisboa  
Departamento de Física, Faculdade de Ciências, Campo Grande, PT-1749-016 Lisboa, Portugal and  
Visiting astronomer, Departament de Física Quàntica i Astrofísica, Institut de Ciències del Cosmos, Universitat de Barcelona  
(ICC-UB), Martí i Franquès 1, E-08028 Barcelona, Spain

FERNANDO COMERÓN

European Southern Observatory, Karl-Schwarzschild-Str. 2, 85748 Garching bei München, Germany  
Version May 27, 2024

## Abstract

We investigate the star formation occurring in the Planck Galactic cold clump PGCC 120.69+2.66. Near-infrared  $JHK_S$  images and  $K$ -band spectroscopy obtained with NOTCam at the Nordic Optical Telescope complemented with archive data are used to study the stellar content. In addition, millimetre line CO and CS spectra were obtained with the Onsala 20 m telescope, and sub-millimetre continuum SCUBA archive data are used to characterise the host molecular cloud. We identify a molecular cloud core traced by CO and CS emission at a distance of 1.1 kpc. In the region studied, we identify 5 submm continuum cores. Embedded in and around these dense submm cores, we find 38 young stellar objects, classified as 9 Class I, 8 Class II, and 21 near-IR excess or variability sources, accompanied by bipolar nebulosities and signs of protostellar jets. Furthermore, a very bright and reddened source is found towards this molecular cloud core. Even though its location appears to suggest its association to the star formation region, its infrared spectral type is compatible with a red supergiant, hidden behind 36 mag of visual extinction.

## 1. INTRODUCTION

Detecting and classifying the young stellar population in molecular clouds at an early star formation phase is vital for the understanding of star formation process - the young stellar objects (YSOs) are the end products and the molecular cloud cores are the initial conditions in which they form. Stars tend to form in groups, often in rich clusters with hundreds to thousands of stars, but also in looser aggregates with fewer young stellar objects (Strom et al. 1993).

The presence of embedded jets and of extended nebular emission often denounces the young stellar character of the associated sources (e.g., McCaughrean et al. 1994; Yun et al. 1997, 2001). Recent large scale studies of nearby star formation regions with infrared surveys (e.g. Evans et al. 2009; Gutermuth et al. 2009; Winston et al. 2020, and references therein) have investigated large populations of embedded YSOs in their early evolutionary phases at high sensitivity and spatial resolution, locating their birthplace to the densest molecular cloud cores, often found distributed along filaments as traced by submm surveys (André et al. 2014).

Based on previous investigations of star formation in the outer Galaxy, selecting IRAS sources with colours

and temperature maps strongly correlated with the presence of embedded infrared protostars or young clusters (Yun et al. 2001; Palmeirim & Yun 2010; Yun et al. 2015), we found that the region around the *IRAS* source IRAS 00267+6511 was a promising candidate for an active star formation site towards the outer Galaxy ( $l = 120.7^\circ$ ,  $b = 2.7^\circ$ ). The region has been identified as a dense cloud core via CO, HCO<sup>+</sup>, and HCN emission (Zhang et al. 2016; Yuan et al. 2016) and is listed in the Planck catalog of Galactic Cold Clumps (Planck Collaboration et al. 2016) derived from three high-frequency bands (353, 545, and 857 GHz). The stellar content had not been studied, given that at optical wavelengths the region is a patch of obscuration against background stars with no sign of star formation. Molecular cloud cores are known to exhibit very high values of visual extinction hiding from optical view both YSOs forming in the cores and other background objects, as well. In fact, in the 2MASS (Skrutskie et al. 2006) near-IR images of the region, we became aware of an intriguingly bright and red object that caught our attention; invisible in optical surveys and situated only 34'' from the IRAS source, i.e. close to the center of the cloud, it could be a very bright YSO or instead a background unrelated source.

We obtained high-resolution near-infrared  $JHK_S$  images and  $K$ -band spectroscopy with the Nordic Optical Telescope (Djupvik & Andersen 2010) to identify and characterise young stellar sources. In addition, we use millimetre and sub-millimetre data, both new and archive data, to define the molecular and dust environment. We report here evidence for early star formation activity in the form of nebular emission, mid- and near-infrared excess sources in the protostellar and pre-main sequence phase. The bright red source appears to be a previously unknown background massive supergiant star hidden behind several tens of magnitudes of visual extinction. Section 2 describes the observations and data reduction, in Sects. 3 and 4 we present and discuss the results, and a summary is given in Sect. 5.

## 2. OBSERVATIONS

### 2.1. Near-infrared observations

Near-IR imaging and spectroscopy was obtained with NOTCam, the Nordic Optical Telescope's near-IR Camera and Spectrograph<sup>1</sup>. The NOTCam detector is a Hawaii 1k HgCdTe IR array and the camera optics has two different scales (Abbott et al. 2000). The wide-field (WF) camera has pixel size of  $0'.234$  and a  $4' \times 4'$  field-of-view, and the high-resolution (HR) camera has a pixel size of  $0'.079$  and a fov of about  $80'' \times 80''$ .

NOTCam imaging has been obtained in free slots in service nights with starting dates 2023-11-23 and 2023-12-28. Due to the extremely red and bright source ( $K_S < 7$  mag), deep broad-band imaging with the WF camera was problematic, and for this filter we needed to add a small cold stop (6 mm) to reduce the transmission to 15%. We also obtained some short exposures with a narrow-band filter (#218) centred on the  $H_2$   $v=1-0$  S(1) line at  $2.122 \mu\text{m}$ . The total on-source exposure times used with the WF camera were 180s (J), 194s (H), 32s ( $K_S + 6\text{mm stop}$ ), and 194s (#218). Two smaller fields mapped with the HR-camera, one to the North (N) and one to the North-West (NW) of the near-IR luminous star, avoiding the bright source, and the total on-source exposure times were 540s in each filter J, H, and  $K_S$  for both of these fields. The seeing measured in these images have PSF fwhm of  $0.4''$  and  $0.6''$  for the N and the NW fields, respectively.

Differential twilight flats were obtained for all filters and domeflats for the combination of  $K$ -band and the 6mm stop. Deeper images were obtained with the HR-camera in the JHKs filters in smaller regions near the bright source. The imaging was obtained with small-step dithers, using ramp-sampling readout and individual exposure times short enough to avoid saturation. The images were reduced with IRAF<sup>2</sup> and the IRAF package notcam.cl v2.6, made for NOTCam image reductions, including bad-pixel correction, flat-field correction, sky evaluation and subtraction, distortion correction, shifting and combination the individual frames.

For each field and filter point sources are detected and measured with aperture photometry, using the IRAF photometry package, applying aperture correc-

tions found using curve of growth on a few bright and isolated stars in each image. We cross-correlated each field with 2MASS sources with quality flag AAA, used to calibrate the NOTCam  $JHK_S$  photometry, as well as the astrometry. The positional rms values are  $0.05''$  and  $0.02''$  for the WF camera and the HR-camera, respectively. The photometric calibration errors of 0.021, 0.027, and 0.054 mag for J, H, and  $K_S$ , respectively, were added in quadrature to the photometric errors obtained in the WF field. For the small HR fields calibration sources were limited to a few stars only. Two stars that overlap in the two small fields observed on different nights scatter by less than  $0.04$  mag in H and  $K_S$  bands and by  $0.12$  in J, the latter most likely due to the faintness in the J-band (18 mag), and we decided to apply  $0.04$  mag as calibration error for the photometry in the HR fields.

The spectroscopy was done with the NOTCam echelle grism Gr#1, the  $K$ -band filter (#208) used as an order sorter, and the  $128 \mu\text{m}$  wide slit (corresponding to  $0'.6$  or 2.6 pixels). This setup covers the range from  $1.95$  to  $2.37 \mu\text{m}$  with a dispersion of  $4.1 \text{ \AA}/\text{pix}$ , giving a spectral resolution  $\lambda/\Delta\lambda$  of about 2100.  $K$ -band spectroscopy of the bright source was obtained on 2023-11-08, dithering along two positions on the slit (A-B) three times to obtain 6 individual spectra, each with an exposure time of 20 seconds (reading out every 4 seconds 5 times in ramp-sampling mode). Calibration lamps were taken while pointing to target to minimize flexure in the wavelength calibration and improve fringe corrections with the spectroscopic flats. To correct the spectrum for Earth's atmospheric features we used as a telluric standard the star HD5071 (SpT B8,  $K_{2\text{MASS}} = 7.49$  mag), observed right after the target. Hot-pixel masks were constructed from darks taken with the same integration time and readout mode. For the target and the standard the individual ABABAB exposures were corrected for hot pixels, flat-field corrected using halogen flats, and sky-subtracted using the neighbouring frame. The individual 1D spectra were optimally extracted and wavelength calibrated using dedicated scripts based on IRAF tasks, after which they were combined to a final spectrum. The target spectrum was divided by the telluric spectrum using the interactive IRAF task *telluric*, having first interpolated over the stellar  $\text{Br}\gamma$  absorption line at  $2.166 \mu\text{m}$  in the telluric. Differential photometry of the telluric in the acquisition image, using three reliable 2MASS stars, gave  $K = 7.56 \pm 0.02$  mag, differing by  $0.07$  mag from the published 2MASS value. This calibration is used to flux-scale a Vega continuum which was multiplied with the target spectrum to correct the slope and give a rough estimate of the target flux.

### 2.2. CO and CS mm line observations

Millimetre single-dish observations of IRAS 00267+6511 were carried out at the 20 m Onsala telescope, in 2009 April. Three maps were obtained in the rotational lines of  $^{12}\text{CO}(1-0)$  (115.271 GHz),  $^{13}\text{CO}(1-0)$  (110.201 GHz), and  $\text{CS}(2-1)$  (97.981 GHz), respectively. The telescope half-power beam width (HPBW) was  $32''$  at 115 GHz and  $38''$  at 98 GHz. The adopted grid spacing was  $30''$  (approximately full-beam sampling). The  $^{12}\text{CO}(1-0)$ ,  $^{13}\text{CO}(1-0)$ , and  $\text{CS}(2-1)$  maps are composed of  $5 \times 5$ , of  $7 \times 7$ , and of  $5 \times 6$

<sup>1</sup> NOTCam is documented in detail at <https://www.not.iac.es/instruments/notcam/>.

<sup>2</sup> IRAF is currently supported and maintained by an IRAF community at <https://iraf.net/>.

pointings, respectively.

A high-resolution 1600 channel spectrometer was used as a back end, with a total bandwidth of 40 MHz and a channel width of 25 kHz, corresponding to approximately  $0.065 - 0.075 \text{ km s}^{-1}$ , at those frequencies. The spectra were taken in frequency-switching mode, recommended to save observational time when mapping extended sources. The antenna temperature was calibrated with the standard chopper wheel method. Pointing was checked regularly towards known circumstellar SiO masers; pointing accuracy was estimated to be better than  $4''$ .

Data reduction followed standard steps: *i*) folding the frequency-switched spectrum; *ii*) fitting the baseline by a polynomial and subtracting it; *iii*) coadding repeated spectra obtained at the same sky position; *iv*) obtaining the main beam temperature  $T_R$  by dividing the antenna temperature  $T_A$  by the  $\eta_{\text{MB}}$  factor, equal to about 0.5 for these lines; and *v*) finally, smoothing the spectra to a velocity resolution of approximately  $0.13 - 0.15 \text{ km s}^{-1}$  at those frequencies. The spectrum baseline RMS noise (in  $T_R$ ), averaged over all map positions, has been found to be 1.4 K for  $^{12}\text{CO}(1-0)$ , 0.4 K for  $^{13}\text{CO}(1-0)$ , and 0.2 K for CS(2-1).

### 2.3. Archive data

This region was surveyed by the Herschel satellite whose database is accessible via the NASA/IPAC Infrared Science Archive (IRSA). It was also observed by the Planck satellite. In this region, the *Planck Early Release Compact Source Catalogue* (Planck Collaboration et al. 2011) lists a submm clump named PLCKECC G120.67+2.66. This catalog was later superseded by the *Planck Catalogue of Galactic Cold Clumps* (Planck Collaboration et al. 2016) containing the source PGCC G120.69+2.66 (with slightly different coordinates). This clump extends by  $11'.6 \times 4'.4$  on the sky. The centre is positioned about 2 arcmin southeast of IRAS 00267+6511, and involves the whole region imaged in this study.

This region was covered by the SCUBA-2 Continuum Observations of Pre-protostellar Evolution Large Program (SCOPE) survey (Eden et al. 2019). The survey was conducted at  $850 \mu\text{m}$  with a beam size of 14.4 arcsec on the James Clerk Maxwell Telescope. We accessed the data base via the Canadian Astronomy Data Centre and downloaded the corresponding FITS image of this region. With a pixel scale of  $4'' \text{ pix}^{-1}$ , it covers about  $10' \times 10'$  encompassing the region mapped by NOTCam and the CO and CS observations.

## 3. RESULTS

### 3.1. The mid-infrared view

We have explored the WISE (Wright et al. 2010) and 2MASS (Cutri et al. 2003) catalogues in the  $4' \times 4'$  region around IRAS 00267+6511 shown in the NOTCam image in Fig. 1. After weeding out extragalactic contaminants and low S/N sources in the WISE sample, we search for Young Stellar Objects (YSOs) among the sources based on their mid-IR Spectral Energy Distributions (SEDs). The standard classification scheme for YSOs is based on the shape of the mid-IR SED quantified by the SED index  $\alpha = d \log \lambda f_\lambda / d \log \lambda$  originally taken from 2 to 10 (or 25)

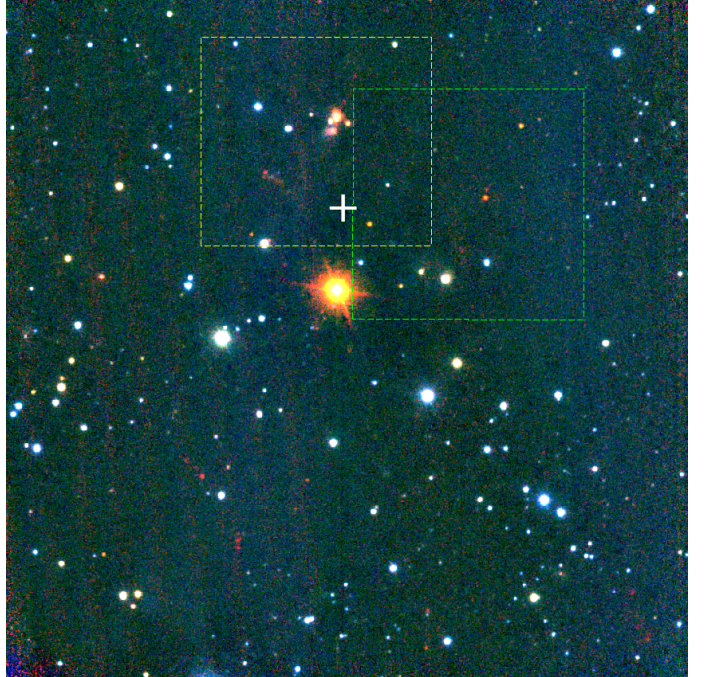


FIG. 1.— NOTCam image of the Planck cold clump PGCC G120.69+2.66 region with the position of IRAS 00267+6511 marked (white plus sign). The image is an RGB composition of J-band (blue), H-band (green) and  $2.122 \mu\text{m}$   $\text{H}_2$  line (red). The FOV is  $4' \times 4'$  with N up and E left. The dashed boxes indicate fields N (yellow) and NW (green) mapped with the high resolution camera in JHKs and shown in Fig. 8. The bright, red star near the centre is discussed in Sect. 4.4.

$\mu\text{m}$  (Lada & Wilking 1984; Greene et al. 1994). A steeply rising SED towards longer wavelengths for protostars embedded in dust envelopes, Class I sources ( $\alpha > 0.3$ ), can be easily separated from a declining slope of the more evolved Class II sources ( $-1.6 < \alpha \leq -0.3$ ) surrounded by circumstellar dust disks. An intermediate range would be occupied by the so-called Flat-Spectrum sources ( $-0.3 < \alpha \leq 0.3$ ). The SED index is frequently translated to colour indices in various magnitude systems that will define IR excess emission above the Rayleigh-Jeans tail of the photospheric black-body. For the WISE photometry in the bands W1 ( $3.4 \mu\text{m}$ ), W2 ( $4.6 \mu\text{m}$ ) and W3 ( $11.8 \mu\text{m}$ ) we apply the criteria described by Koenig & Leisawitz (2014) for removing extragalactic contaminants as well as defining the Class I and Class II sources according to their location in the  $[3.4] - [4.6] / [4.6] - [12]$  colour-colour diagramme. Following their criteria we discard more than 80% of the sources in the field as contaminants and find 17 YSOs with mid-IR excess and classify them as Class I and Class II sources as shown in Fig. 2. The 9 Class I sources are marked with red circles while the 8 Class IIs are marked with green squares. See Table 3 for details about the Class I and Class II YSOs.

### 3.2. The near-infrared view

Figure 1 shows a color-composed image from broadband filters J (blue), H (green), and a narrow-band filter centred on the  $2.122 \mu\text{m}$   $\text{H}_2$  line (red) of the  $4' \times 4'$  region around IRAS 00267+6611 obtained with the NOTCam WF camera. Because of the very red and bright source in the centre of the field, only very short exposures were obtained to avoid saturation of the detector. The 2MASS

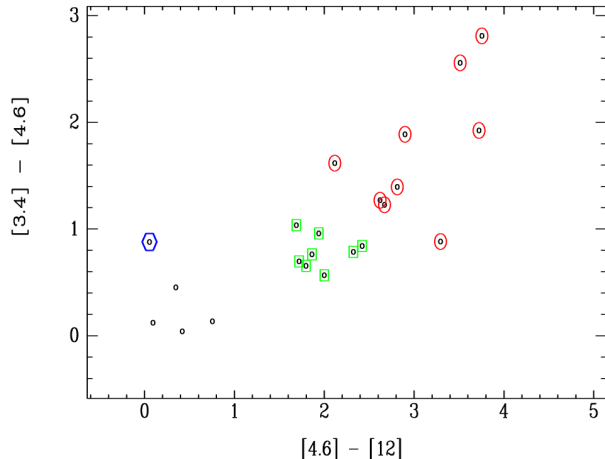


FIG. 2.— WISE  $[3.4]-[4.6]/[4.6]-[12]$  colour-colour diagramme showing the Class I sources (red) and Class II sources (green) inside the  $4' \times 4'$  FOV. The blue hexagon marks the position of the brightest near-IR source in the region, a candidate red supergiant, see Sect. 4.4.

sources in this region are shown in a  $J - H/H - K_S$  diagramme in Fig. 3. The loci of unreddened main-sequence stars, giants and supergiants are indicated with a solid (violet), a dotted (red), and a dash-dot (blue) curve, respectively, based on their intrinsic near-IR colours tabulated in the compilation of Tokunaga (2000). We have adopted the near-IR extinction law  $A_\lambda \propto \lambda^{-2.07}$  recommended by Wang & Chen (2019) to be the best average global extinction law in the wavelength range 1 - 3.3  $\mu\text{m}$ . This gives a reddening slope in the  $J - H/H - K_S$  diagramme for the 2MASS filters of 2.0, which is depicted with a dashed line that shows the reddening vector of an A0 star. We note that for highly reddened objects the extinction law follows a curve in this diagram (Kaas 1999), as shown by the full-drawn line, where deviations away from the slope is given for the 2MASS colours by Stead & Hoare (2009). One particular object in this diagram is sufficiently reddened that this deviation is not insignificant. This is the source marked by a blue square, the very brightest object in the  $K_S$  band, see description in Sect 4.4. The previously classified YSOs from the WISE data are high-lighted in this diagramme with red circles (Class Is) and green squares (Class IIs). These sources are listed in Table 3.

To further explore the YSO content in the region we use the  $J - H/H - K_S$  diagramme to search for near-IR excess. Bona-fide near-IR excess sources are defined as those that are displaced to the right and below the reddening vector by more than  $2\sigma$  the errors in the colour indices. We find 2MASS near-IR excesses in 6 of the previously classified YSOs with WISE, but only one additional near-IR excess source is found, however, and the reason for this is the lack of valid entries for the magnitude errors in all JHK<sub>S</sub> bands. Some of the sources located in the near-IR excess region therefore do not qualify as bona-fide near-IR excess sources. For these we use instead the photometry from the short exposure NOTCam WF-camera JHK<sub>S</sub> images, and in addition, we use the two smaller fields observed with the HR-camera, their locations are marked in Fig. 1 with dashed yellow and green lines and the images are shown in Fig. 8. Due

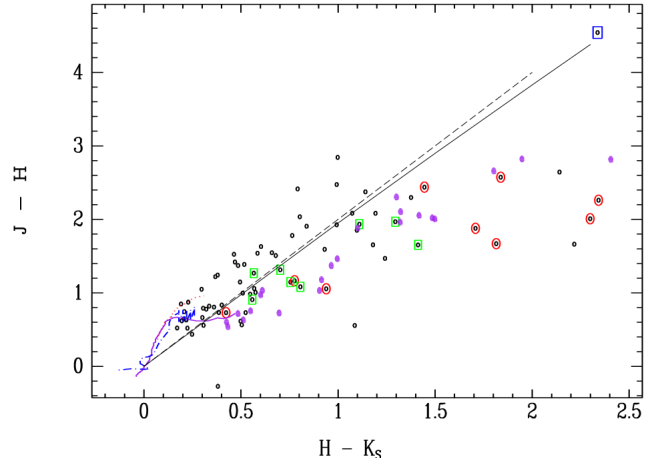


FIG. 3.— Near-IR  $J - H/H - K_S$  diagram of 2MASS sources (black circles) where the previously classified Class Is (red) and Class IIs (green) from WISE colours are marked. Additional near-IR photometry from NOTCam WF and the two HR fields that give near-IR excess are added (violet dots). For reference, the very bright and red source in Fig. 1, is indicated with a blue square and discussed in Sect. 4.4.

to high extinction there are very few detections in the  $J$  band compared to the  $K_S$  band, and this limits the depth to which we can search for near-IR excess sources. Many of the sources with a large  $H - K_S$  colour index but no detectable  $J$ -band fluxes could be fainter YSOs embedded in the cloud, and some are already found to be Class Is using WISE, but the lack of  $J$ -band photometry does not allow us to reliably distinguish between near-IR excess and reddened background objects. For the NOTCam sample we apply a similar criterion for near-IR excess as above, but we use a less steep reddening slope of 1.7 for the  $J - H/H - K_S$  diagramme, calculated for the NOTCam filters using the same extinction law (Wang & Chen 2019). The NOTCam photometry detects near-IR excesses in several of the previously found Class I and Class II sources and reveals 14 additional sources that we suggest as YSO candidates based on excess emission at 2  $\mu\text{m}$ . These are tabulated in Table 4, and we have added them as violet dots to the 2MASS  $J - H/H - K_S$  diagramme in Fig. 3.

When comparing the photometry obtained with 2MASS and NOTCam some stars stand out as clearly variable. Adding the magnitude errors in each band from 2MASS and NOTCam in quadrature, sources that have deviations larger than  $3\sigma$  are flagged as variable. Among 74 common sources 20 had varied by more than  $3\sigma$  in one of the bands, while 8 sources have varied in two or more bands. Among the variables are 3 Class Is, 3 Class IIs and 5 near-IR excess sources.

Using variability as a YSO criterion is tempting, as young stars are prone to vary, but some of the variations we see could be related to the different spatial resolution of the samples causing blending. In order to weed out false positives we tested the YSO candidates against Gaia (Gaia Collaboration et al. 2016) proper motions. The Gaia DR3 catalogue (Gaia Collaboration et al. 2023) lists 57 sources in the  $4' \times 4'$  area of our study. Many YSO candidates are not detected due to being embedded or highly extinguished, but proper motions were found

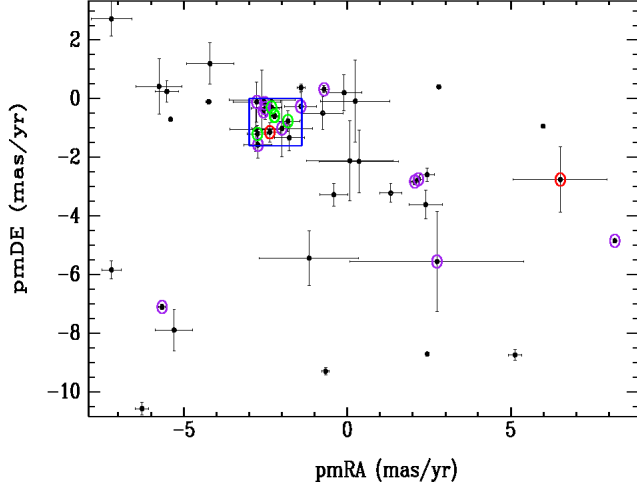


FIG. 4.— Proper motions of the 57 Gaia DR3 detected stars within the  $4' \times 4'$  region of our study (black dots with errorbars). The YSO candidates detected are colour coded as follows: red for the single Class I source, green for 4 Class II sources and violet for 13 near-IR excess or variability candidates. Most YSO candidates cluster in the blue box.

for 2 of the Class Is, 5 of the Class IIs and 13 of the sources selected on the basis of near-IR excess or variability. Figure 4 shows the proper motion distribution of all Gaia sources in the region (black dots with error bars), whereas the YSO candidates are encircled with colour codes. Most of the YSOs cluster around similar proper motions outlined by the blue box. The box area has been defined by the individual error bars of one Class I and 5 Class II sources, and inside the box we find 16 sources. Their median proper motions are  $-2.4 \text{ mas yr}^{-1}$  and  $-0.6 \text{ mas yr}^{-1}$ , for pmRA and pmDE, respectively. The scatter in the proper motions of these sources is  $0.41$  and  $0.48 \text{ mas yr}^{-1}$  in pmRA and pmDE, respectively, which is of the same order as the individual Gaia measurement errors, the mean error being  $0.43 \text{ mas yr}^{-1}$ . Thus, we can not use the proper motion scatter to extract a YSO velocity dispersion. Regarding the variability criterion, we find that 6 variable candidates have deviating proper motions and are discarded, leaving 7 variability selected YSOs of which four are not detected by Gaia. We add these to the near-IR excess sources, giving a total of 21 YSO candidates from near-IR photometry, see Table 4. Surprisingly, one Class I source has a deviating proper motion. We note that this is the faintest of all the Class Is at  $22 \mu\text{m}$  and it is situated outside the Scuba cores (cf. Fig. 7). All the YSOs with Gaia measurements have large errors in their parallaxes, except for two of the Class IIs we use to estimate the distance (cf. Sect. 4.1).

The final sample of YSOs in the region is shown in Fig. 7 overlaid on a submm map from Scuba/JCMT at  $850 \mu\text{m}$ , showing the dense cores in the region. The Class I protostar positions are marked with large red circles, Class II sources with green squares, near-IR excess sources with orange crosses and variable sources with cyan diamonds.

### 3.3. Millimetre emission

Figure 5 shows the  $^{12}\text{CO}(1-0)$ , the  $^{13}\text{CO}(1-0)$ , and the  $\text{CS}(2-1)$  spectra taken towards IRAS 00267+6511 ((0,0) position of the map). The spectra all peak at

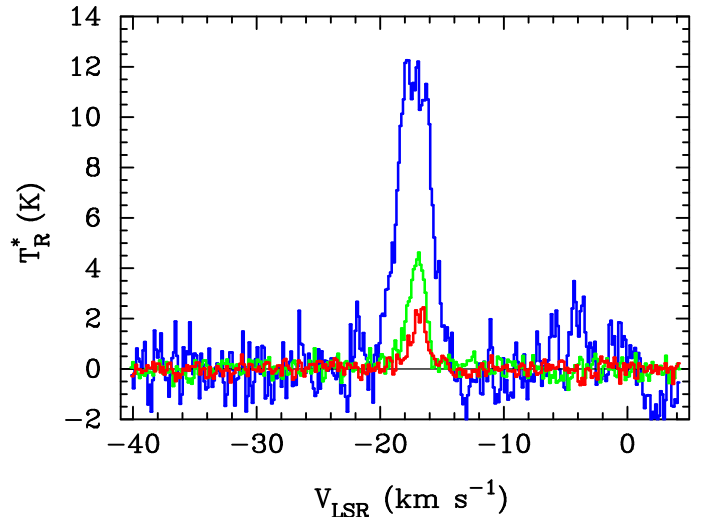


FIG. 5.— Spectra of the three observed molecular transitions towards the IRAS source ((0,0) position of the maps):  $^{12}\text{CO}(1-0)$  (blue),  $^{13}\text{CO}(1-0)$  (green),  $\text{CS}(2-1)$  (red).

about  $-17.0 \text{ km s}^{-1}$ , a value that can be adopted as the velocity of the gas component associated with the young stellar sources, and are consistent with the global radial velocity of PGCC G120.67+02.66 quoted by Zhang et al. (2016) in their CO survey of Planck cold cores in the second Galactic quadrant. They have mapped this region and detected strong CO emission. The CO lines were found at  $V_{\text{LSR}} = -17.56$ , with velocity resolution of  $0.17 \text{ km s}^{-1}$ .  $\text{HCO}^+$  and  $\text{HCN}$  emission have also been detected (Yuan et al. 2016). Our detection of CS emission confirms the presence of high volume density gas in this region.

#### 3.3.1. CO and CS emission

The  $^{12}\text{CO}(1-0)$  maps (both intensity and integrated intensity, not shown) reveal no remarkable features apart from strong emission with little spatial variation. However, the values of  $^{12}\text{CO}(1-0)$  emission, even though it is usually optically thick, can be used to derive a first estimate of the optical visual extinction  $A_V$  in the line-of-sight of the  $^{12}\text{CO}(1-0)$  beams. This estimate is based on the empirical correlation between the  $^{12}\text{CO}(1-0)$  integrated intensity and the  $\text{H}_2$  column density along the line of sight,  $N_{i,j}$ , at position  $(i, j)$ :

$$N_{i,j}(\text{H}_2) = X \int T_R dv \quad (\text{cm}^{-2}), \quad (1)$$

together with the relation  $N(\text{H}_2)/A_V = 9.4 \times 10^{20} \text{ cm}^{-2} \text{ mag}^{-1}$  (Frerking et al. 1982).

The constant  $X$  has been determined empirically by various works. Adopting the value used by May et al. (1997) for the outer Galaxy, of  $X = 3.8 \times 10^{20} \text{ cm}^{-2} (\text{K km s}^{-1})^{-1}$ , we obtain a first estimate of  $A_V = 20 \text{ mag}$ .

Figure 6 presents the contour maps of  $^{13}\text{CO}(1-0)$  integrated intensity and  $\text{CS}(2-1)$  intensity (black lines) towards IRAS 00267+6511 superimposed on  $4' \times 4'$  NOT-Cam  $H$ -band images. Both transitions peak about  $0.7$  arcmin southwest of the IRAS source revealing the presence of a molecular cloud core with high column densities and high volume densities in this region. This core is part

TABLE 1  
SCUBA CORES IN THE REGION AROUND IRAS 00267+6511.

Number	Name	$\Delta$ R.A. (arcmin)	$\Delta$ Dec (arcmin)	Effective radius (arcmin)	Integrated flux (Jy)	Core mass ( $M_{\odot}$ )
1	G120.652+2.681	-0.78	-0.48	0.44	2.31 (0.23)	140
2	G120.668+2.691	0.02	0.45	0.47	2.15 (0.20)	130
3	G120.676+2.658	0.74	-1.75	0.37	1.57 (0.16)	96
4	G120.655+2.645	-0.45	-2.62	0.20	0.38 (0.04)	23
5	G120.689+2.678	1.42	-0.48	0.11	0.16 (0.01)	9.7

of the source named PGCC G120.67+02.66 and mapped in  $^{12}\text{CO}$  and  $^{13}\text{CO}$  by Zhang et al. (2016), here mapped with higher angular resolution.

Around the peak of  $^{13}\text{CO}$  emission, there is a relatively slow decrease, with an extended plateau of emission where column densities remain high. The bright red-dened star lies at a position within this plateau. Using the value of the  $^{13}\text{CO}$  emission, under the assumptions of optically thin and LTE conditions, we derive a value of  $A_V = 6$  mag at the position of this star. This is clearly a lower limit, because in regions of high extinction the  $^{13}\text{CO}(1-0)$  transition is not optically thin and the calibration methods (e.g. Frerking et al. 1982), that were derived for small values of  $A_V$ , do not lead to accurate results when applied in the presence of large values of visual extinction.

The CS intensity map displays a single strong peak of emission at approximately the same map position as the peak on the  $^{13}\text{CO}$  map. However, unlike  $^{13}\text{CO}(1-0)$ , away from the CS peak the emission exhibits a strong gradient in all directions around an elongated, approximately elliptical core with major axis oriented close to the NE-SW direction.

The YSOs identified on the infrared images lie in regions of the  $^{13}\text{CO}$  and CS maps around the plateau and the peak of maximum emission. Most Class I sources are located closer to the peaks of emission (see also Fig. 7), in regions of higher density.

### 3.3.2. Planck Galactic Cold Clumps and SCUBA cores

Analysis and photometry of the 850  $\mu\text{m}$  SCUBA-2 image resulted in the identification of five sub-mm sources in the region covered by our near-infrared NOTCam images. They are listed in Table 1 (positions relative to IRAS 00267+6511, effective sizes, and 850  $\mu\text{m}$  fluxes).

The three brightest and more extended sources are also marked by blue dashed lines on Fig. 6. They were also detected by the Herschel satellite at 250, 350, and 500  $\mu\text{m}$ , where the first two brightest are seen as bright sources at all three wavelengths, and the third source is much fainter. In addition, the large scale Herschel images reveal that these cores are part of a filamentary structure that include filaments that cross at the location of these cores (hub filaments).

The two brightest SCUBA cores have positions on each side of the peak of the CS map along the major axis of the elliptical CS core (Fig. 6). The brightest core (#1 in Table 1), also appears to be the densest: its location coincides with the reddest WISE source, and with the peaks of the  $^{13}\text{CO}$  and CS integrated intensity maps. Furthermore, it is the region where the CO and CS spectral lines exhibit larger line widths. Core #2 coincides with the IRAS position. The two brightest SCUBA cores roughly

cover the NOTCam HR fields N and NW, respectively, seen in Fig 7.

Because dust continuum emission at sub-mm wavelengths is optically thin, we can estimate the masses of the SCUBA cores. Under the assumption of constant dust temperature, the dust mass can be obtained using:

$$M_{\text{dust}} = \frac{S_{\lambda}}{\kappa_{\lambda} B_{\lambda}(T_d)} D^2$$

where  $S_{\lambda}$  is the 850  $\mu\text{m}$  flux,  $T_d$  is the dust temperature ( $T_d = 12.6$  K, Planck Collaboration et al. (2016)). We adopted a distance of 1.1 kpc (See Sect. 4.1), a dust-to-gas ratio of 1%, and a spectral index  $\beta = 2$  for the emissivity law  $\kappa_{\lambda} \propto \lambda^{-\beta}$ , with  $\kappa_{1\text{mm}} = 0.3 \text{ cm}^2 \text{ g}^{-1}$ . The derived mass of the SCUBA cores are given in the last column of Table 1.

## 4. DISCUSSION

### 4.1. Distance

From the spectral lines, we derive the kinematic heliocentric distance, using the peak radial velocity. This can be done using different methods namely, e.g. applying the circular rotation model by Brand & Blitz (1993), or using the Reid et al. (2014) rotation curve with the Reid et al. (2019) updated Solar motion parameters, possibly including Monte Carlo methods (e.g. Wenger et al. 2018), among others. Using the conventional solar motion parameters, and with  $V_{\text{LSR}} = -17 \text{ km}^{-1}$ , a distance of 1.5 kpc is obtained, not far from the value of 1.75 kpc derived by Zhang et al. (2016) using the Sofue (2011) method. Zhang et al. (2018) using a Bayesian calculation derive a distance of  $0.90 \pm 0.29$  kpc to G120.67+02.66. However, if we adopt the Reid et al. (2014) rotation curve together with the revised values of the Galactic constants  $R_0$  and  $\Theta_0$  of Reid et al. (2019), we derive distances between 0.95 and 1.25 kpc. Interestingly, Guo et al. (2020) use data from extinction catalogues and parallaxes from Gaia DR2, together with modelling, and derive distances to Planck Galactic cold cores. They obtained a distance of  $1063 \pm 104$  pc to PLCKECC G120.67+02.66. Furthermore, we find that among the 8 Class II sources found in Sect. 3.1, as many as 5 have measured parallaxes in the GAIA DR3 catalogue (Gaia Collaboration et al. 2023), and two of these have relatively small errors. These two optically visible Class IIs are located relatively close to the center of the region, and we use their parallaxes at  $0.867 \pm 0.025$  mas and  $0.948 \pm 0.097$  mas to estimate a distance of  $1.1 \pm 0.05$  kpc. We conclude that the currently best estimate for the distance to this star formation region and molecular cloud core is 1.1 kpc.

### 4.2. The embedded YSO population

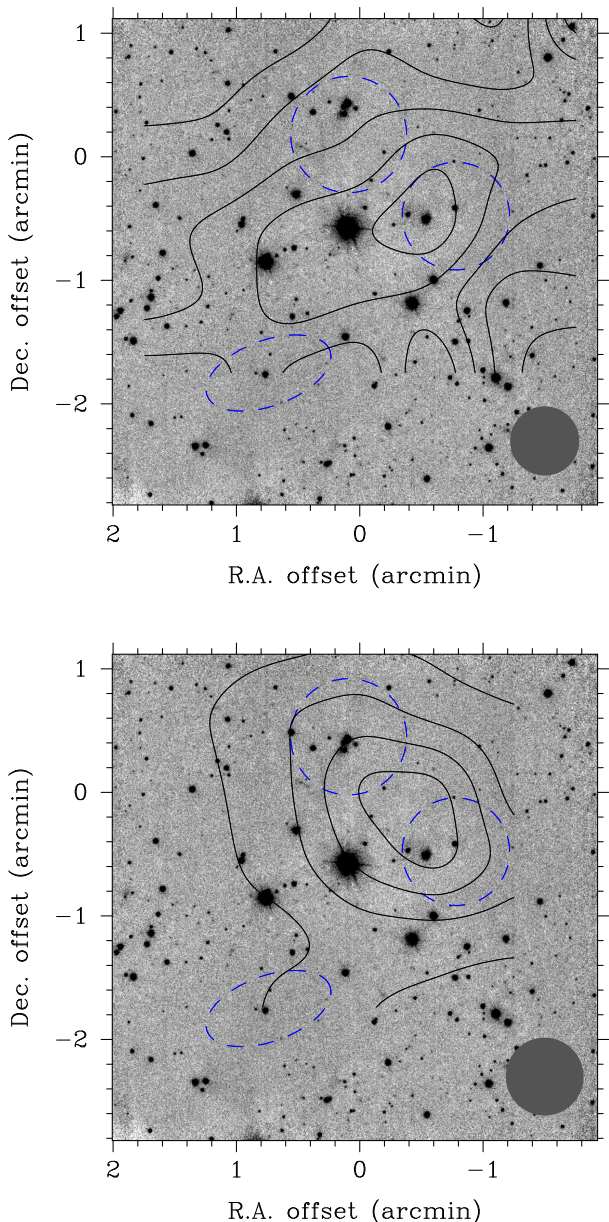


FIG. 6.— Smoothed contour maps of millimetre emission towards IRAS 00267+6511 superimposed on the NOTCam H-band image: (*top*)  $^{13}\text{CO}(1-0)$  integrated intensity: the lowest contour is at  $6 \text{ K km s}^{-1}$ , subsequent contours are in steps of  $0.8 \text{ K km s}^{-1}$ ; (*bottom*):  $\text{CS}(2-1)$  intensity: the lowest contour is at  $1.0 \text{ K}$ , subsequent contours are in steps of  $0.4 \text{ K}$ . The offsets are relative to the position of the IRAS source. The solid circle represents the telescope main beam. Notice the presence of a high column density peak and plateau on the  $^{13}\text{CO}$  map, and a high volume density core on the CS map, both about  $0'.7$  southwest of the IRAS source. The blue dashed contours represent the approximate locations and extents of the three brightest SCUBA cores detected towards this region (see later in the text).

The results from exploring the stellar population with mid-IR WISE and near-IR 2MASS and NOTCam photometry as explained in Sect. 3.1 and Sect. 3.2 demonstrate a rich collection of young stars with 9 Class I sources, 8 Class II sources, and 21 YSO candidates from the near-IR study. The total sample of 38 YSOs is shown in Fig. 7 overlaid on the  $4' \times 4'$  H-band image which for a distance of 1.1 kpc corresponds to an area of  $1.3 \text{ pc} \times 1.3 \text{ pc}$ , giving an average stellar surface density of

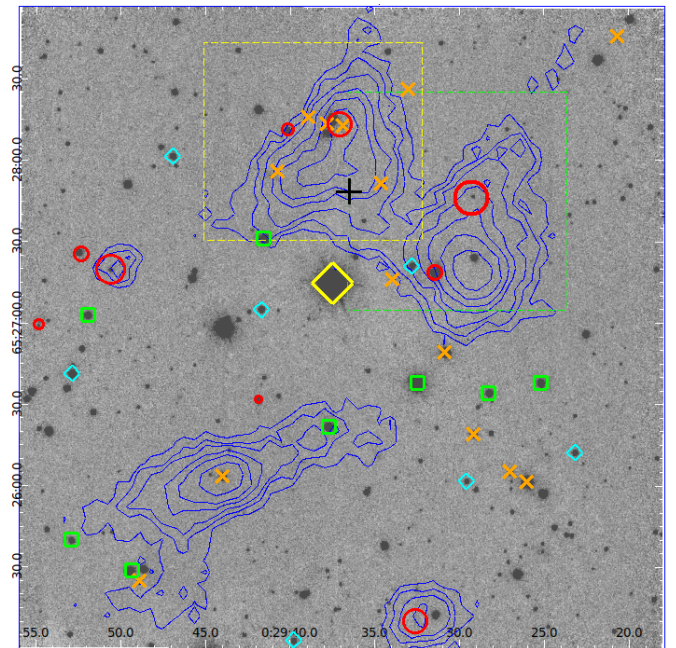


FIG. 7.— The YSO sample overlaid on the H-band image with the position of IRAS 00267+6511 marked (black plus sign). The blue contours are Scuba  $850 \mu\text{m}$  continuum emission shown in steps of 0.2, 0.3, 0.4, 0.6, 0.8, 1.1 and  $1.6 \text{ mJy per square arcsec}$ . Class I sources (red circles, where size suggests relative brightness at  $22 \mu\text{m}$ ) and Class II sources (green squares) as selected from the WISE mid-IR colours, near-IR excess sources (orange crosses) and variable sources (cyan diamonds) as selected from the various sets of NOTCam and 2MASS photometry. The yellow diamond shows the location of the bright infrared source that may be a background supergiant. The dashed boxes outline the small regions imaged with the NOTCam high-resolution camera and are shown in Fig. 8.

$24 \text{ YSOs pc}^{-2}$ . This would meet the criterion of a stellar cluster as defined in Lada & Lada (2003), but is lower than the limit of  $200 \text{ YSOs pc}^{-2}$  used to define a cluster by Gutermuth et al. (2005). The contours in Fig. 7 show the high spatial resolution  $850 \mu\text{m}$  mapping from Scuba/JCMT that outlines the dense cores listed in Table 1. We note that all cores are populated with YSOs, and that most Class Is are embedded in a core. Even the two smallest cores have a Class I source inside the density contours. While the spatial distribution of the YSOs in general is relatively scattered, the Class I sources are essentially located in the cores and the remaining YSOs partly in the submm cores and partly outside.

The number ratio Class I/Class II is a measure of activity and youth since the average lifetime of the Class I stage is estimated to  $0.4 \text{ Myr}$  (Evans et al. 2009) and the duration of the Class II phase is typically taken to be 2-3 Myr (see also Dunham et al. 2015). This means that a number ratio around unity suggests the region is extremely young with on-going formation of protostars. Such high ratios are typical in environments of tight stellar groups according to the *Spitzer* based study of the solar neighbourhood (Evans et al. 2009). Gutermuth et al. (2009) finds a median Class I/Class II ratio of 0.27 in 36 star-forming cores within 1 kpc of the Sun. The 21 YSO candidates from the near-IR study can not be classified as bona-fide Class IIs, but most are likely pre-main sequence disk sources, although Fig. 3 shows that some have very red  $H - K_S$  indices and occupy the region of

Class Is. If we would add the 21 sources to the Class II category, the number fraction becomes 9/29 which is still high. Another indication of youth is the location of the YSOs with respect to their birthplaces, presumably in the cores. If we adopt a stellar velocity dispersion of  $0.9 \text{ km s}^{-1}$ , which is the value measured for the young embedded stellar cluster NGC 1333 (Foster et al. 2015), this would disperse the YSOs by as much as 0.9 pc in 1 Myr. These considerations suggest that the age of this star formation region is likely below 1 Myr.

Given the embeddedness and the very early stage of star formation, we have not attempted to determine the masses of the YSOs.

The SCUBA core #2 in Table 1 (G120.668+2.691, the northern-most in Fig 7) contains 8 identified YSOs, including two Class I protostars, and is the core richest in detected YSOs. For a 1.1 kpc distance the effective core radius is 0.15 pc, giving a stellar surface density of  $113 \text{ YSOs pc}^{-2}$ , which is similar to that of the central cluster (A) in the Serpens Cloud Core measured within an edge of  $A_V = 20 \text{ mag}$  (See Harvey et al. 2007, Table 6, adjusted to  $d=415 \text{ pc}$ ). Assuming symmetry in the radial direction, the volume density in this core is  $570 \text{ YSOs pc}^{-3}$ . This fits well with the definition of a tight stellar group ( $> 25 M_\odot \text{ pc}^{-3}$ ) by Evans et al. (2009) even if we would assign a low average stellar mass. If we assume that the mean YSO mass is  $1 M_\odot$  and use the estimated core mass in Table 1, the present star formation efficiency (SFE) in this core reaches  $\sim 6\%$ .

#### 4.3. Extended emission in the dense cores

SCUBA core G120.668+2.691 (#2 in Table 1) is imaged at high-resolution in the near-IR in field *N* shown in the left panel of Fig. 8. This core contains a nebulosity with emission extending out from a dark center forming an hour-glass shaped nebula, which is seen in our images to extend over at least  $7''$  across the sky, corresponding to  $\sim 8000 \text{ AU}$ . The structure is seen in all three JHK<sub>S</sub> filters, is strongest in the K<sub>S</sub> band, and reddest in the northern part. The inner region of the northern cone has a sharp peak which is, however, not a point source as it is slightly more extended ( $\text{fwhm} = 0.7''$ ) than the stellar PSF ( $\text{fwhm} = 0.4''$ ). The intensity in this peak in the K<sub>S</sub> band is 10 times that of the southern cone. Such a morphology can be interpreted as scattered light from cavities formed as a bipolar jet/wind/outflow from a protostar has begun to clear the dust cocoon in the polar regions. Although at a lower spatial resolution, this object looks remarkably similar to the nearby Class 0 protostar L 1527 IRS as imaged by NIRC*am* at the James Webb Space Telescope (See Fig.1 in Tobin & Sheehan 2024). We interpret the nebula as being mainly scattered light, although some H<sub>2</sub> line emission is seen in the narrowband images. In the colour coded image in Fig. 1, however, the presence of a few very faint knots of H<sub>2</sub> line emission (red) is suggested along the northern axis. These knots could be signs of shocked molecular gas from a protostellar jet.

A zoomed-in image of the hour-glass nebulosity is shown in the right-hand panel of Fig. 8 with the coordinates of the Class I source J002937.06+652813.1 from the WISE catalog marked. It is offset from the near-IR source next to it; the 2MASS cross-correlation measure gives an offset of  $1.45''$  together with an extended

source flag of 5, which means it falls within  $5''$  of an extended 2MASS source. Taking into account the WISE spatial resolution of  $6''$  and the high YSO density, the Class I source is likely the driving source giving rise to the nebula, having its catalog coordinates confused with the 2MASS extended source and the near-IR point source to the west.

Further to the South in field *N* several features of faint and red extended emission are seen. One particular structure is an NE/SW elongated nebulosity that looks like parts of a fragmented jet, but what could be its originating source is not obvious.

Most of SCUBA core G120.652+2.681 (#1 in Table 1) is covered by field *NW* and shown in the middle panel of Fig. 8. This is a very dense region and we detect only 4 YSOs (cf. Fig. 7), but it includes the brightest  $22 \mu\text{m}$  source, a Class I protostar that is deeply embedded and has an equally red but fainter neighbour. Another Class I in this core is located in a group of YSOs in the lower part of the image and has some extended emission. The blue coloured star located near the peak of the dense submm core is a foreground object.

The southern of the three largest SCUBA cores (#3, G120.676+2.658), is more elongated and Fig. 7 shows that five YSOs are related to it, none of them bona-fide Class I sources. From the large view in Fig. 1 we see a structure of several knots (red colour, i.e. narrowband  $2.12 \mu\text{m}$  H<sub>2</sub> line emission) extending out from the near-IR source that is located at the peak of the dust continuum emission. We believe this is a molecular hydrogen object (MHO) owing to shocked gas from a bipolar jet, with a projected orientation perpendicular to the elongated core. Higher S/N imaging in narrow-band filters on and off the H<sub>2</sub> line is required to properly characterize the jet.

#### 4.4. A red supergiant star?

The brightest source in the infrared images, both in Fig. 1 and in the WISE atlas is the source 2MASS 00293749+6527146 aka WISE J002937.50+652714.7, a hindrance for deep near-IR imaging due to its strong *K* band brightness. It is located close to the centre of the region, has an extremely red colour in the near-IR, while nothing is seen in the optical except for a marginal detection in the PanSTARRS DR1 *y*-band image, and it is not in the Gaia DR3 catalogue. In the near-IR colour-colour diagram in Fig. 3 the location of the source (open blue square) is consistent with it being a highly reddened supergiant or giant. In the WISE CC diagram in Fig. 2 the source has excess emission in the  $[3.4] - [4.6]$  index but not in the  $[4.6] - [12]$  index. It also has a clear excess in a  $K_S - [3.4]/[3.4] - [4.6]$  diagram, where it occupies a locus similar to that of the Class II sources, but according to the criteria of Koenig & Leisawitz (2014) the source would be rejected as a YSO because it is too bright at  $3.4 \mu\text{m}$ , as it by their definitions would enter the locus typically occupied by AGB stars. The source was also observed by the Midcourse Space Experiment (MSX), and the A band ( $8.28 \mu\text{m}$ ) flux in the MSX6C point source catalogue (Egan et al. 2003) is  $0.59 \pm 0.02 \text{ Jy}$  which translates to  $A = 4.99 \text{ mag}$  using  $58.49 \text{ Jy}$  for zeroth magnitude (Egan et al. 1999).

The NOT*Cam* photometry obtained in 2023 shows



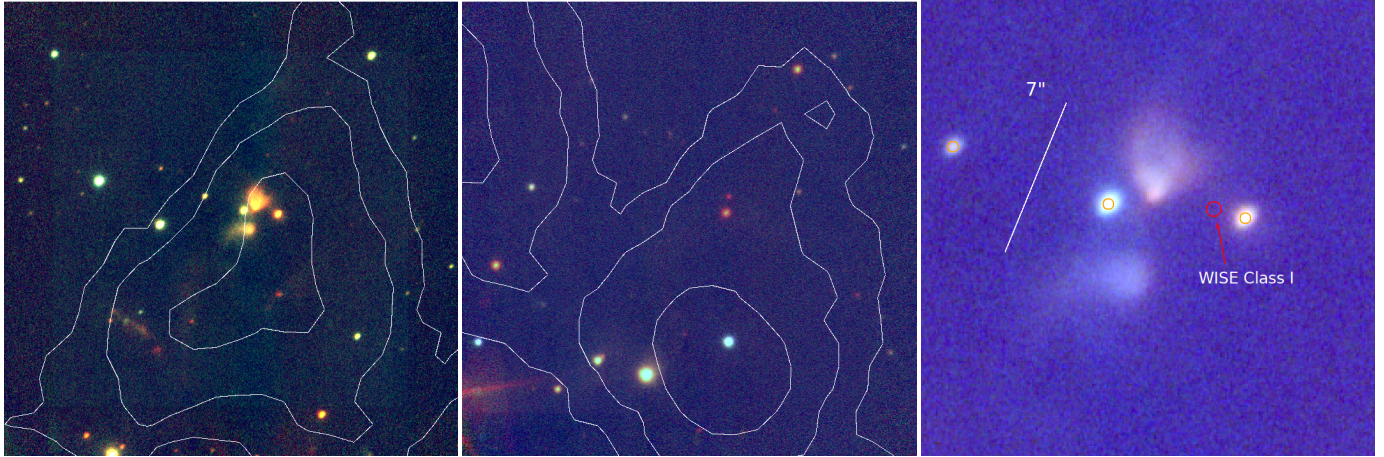


FIG. 8.— NOTCam HR-camera imaging of the two smaller fields *N* (left) and *NW* (middle), both  $80'' \times 80''$  ( $0.43 \times 0.43$  pc) with *N* up and *E* left, and RGB colours: J (blue), H (green) and  $K_S$  (red). The  $850 \mu\text{m}$  emission (white contours) in steps of 0.2, 0.4, and  $1.0 \text{ mJy}$  per square arcsec. A blow-up of the hour-glass shaped nebulosity in field *N* is shown (right) with the spatial scale and the tabulated position of the WISE Class I source (red circle) and three near-IR excess sources (orange circles) indicated.

TABLE 2  
IR PHOTOMETRY OF THE RED SUPERGIANT CANDIDATE.

	J (mag)	H (mag)	$K_S$ (mag)	
2MASS	$13.77 \pm 0.03$	$9.23 \pm 0.03$	$6.89 \pm 0.02$	
NOTCam	$13.97 \pm 0.02$	$9.54 \pm 0.03$	$7.09 \pm 0.05$	
	[3.4] (mag)	[4.6] (mag)	[12] (mag)	[22] (mag)
WISE	$6.06 \pm 0.10$	$5.19 \pm 0.07$	$5.13 \pm 0.02$	$4.61 \pm 0.03$

that the source has faded by about 0.2 mag in all bands since the 2MASS measurement obtained in 1999, see Table 2. The MSX A band variability flag indicates that the source has varied over the course of the MSX mission (1996-1997) by more than  $3\sigma$ . The *WISE* variability flag is 2 for the [3.4] and [4.6] bands, which means a small probability of being variable in the three epochs over the *WISE* mission.

A K-band spectrum of the source is shown in Fig. 9. Its prominent and deep CO bandhead absorptions at  $2.2935 \mu\text{m}$  ( $2-0$ ),  $2.3227 \mu\text{m}$  ( $3-1$ ), and  $2.3535 \mu\text{m}$  ( $4-2$ ) together with the absorptions of the Ca I triplet around  $2.263 \mu\text{m}$  and the Na I doublet around  $2.207 \mu\text{m}$ , and no appreciable  $\text{Br}\gamma$  at  $2.166 \mu\text{m}$ , concur to indicate a late spectral type. We measure the equivalent widths as described in Comerón et al. (2004) and find the EWs of the Na I doublet ( $2.2062, 2.2090 \mu\text{m}$ ) to be  $5.1 \text{ \AA}$  and the Ca I triplet ( $2.2614, 2.2631, 2.2657 \mu\text{m}$ ) to be  $4.7 \text{ \AA}$ . The reference continuum was measured on both sides of the features and the errors are estimated to be  $< 1 \text{ \AA}$ . We have measured the EW of the  $2.29 \mu\text{m}$  CO ( $2-0$ ) absorption feature from  $2.2920$  to  $2.3020 \mu\text{m}$ , i.e. over wavelength range of  $0.010 \mu\text{m}$ , using reference continuum levels on the blue side of the feature extrapolated to the red side, and we find  $\text{EW}_{\text{CO}(2-0)} = 25.5 \pm 1 \text{ \AA}$ . These measured EWs are very similar to those measured for red supergiants (e.g. Comerón et al. 2004, 2016). Using the relation between spectral type and the EW of CO ( $2-0$ ) established in Davies et al. (2007), which is based on the spectral type versus temperature calibration of Levesque et al. (2005), a tentative IR spectral type of M2 I can be assigned to the target. We caveat that a later M-type

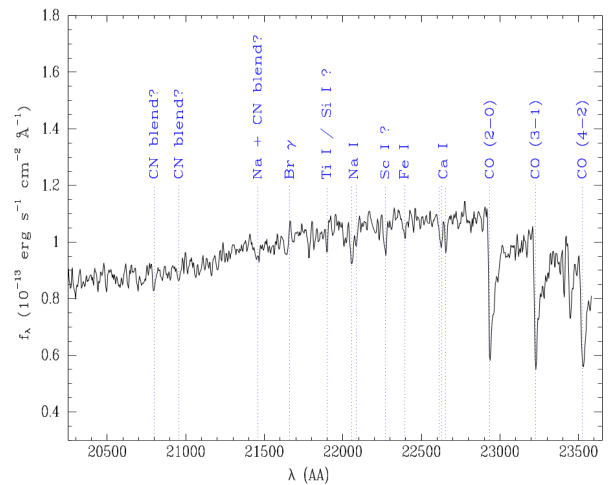


FIG. 9.— NOTCam K-band spectrum of the red luminous star showing the telltale signature of a late type star; very strong CO bandhead absorptions, as well as the Ca I triplet at  $2.263 \mu\text{m}$  and the Na I doublet at  $2.207 \mu\text{m}$  in absorption.

giant could also reach similarly deep CO absorptions, although in that case the water steam bands are often prominent, and we do not see any notable depression shortwards of  $2.1 \mu\text{m}$  in this target. Comparison was made with the near-IR spectral atlases by Wallace & Hinkle (1997) and Lançon & Wood (2000). With help of the online archive of spectra of luminous cool stars in numerical form provided by Lançon & Wood (2000), we could measure the EW of the  $2.29 \mu\text{m}$  CO feature in the same manner as for our target for two M2 supergiants and one M5.5 giant and find that our target has an EW in between the two types.

The star's auspicious position at the very centre of the star formation region raises the question of whether it could be an embedded outburst object. We can probably exclude that it is an FU Orionis outburst, although they present similarly deep CO absorption bands and are often bluer when in outburst (Szegedi-Elek et al. 2020), because its luminosity would be an order of magnitude larger than what is typical for FUORs, and furthermore,

the Na I and Ca I absorptions in the K-band spectrum are too strong for such an interpretation (Connelley & Reipurth 2018).

According to Elias et al. (1985) the intrinsic  $H - K_S$  colour for the M2 I spectral type is  $(H - K_S)_0 = 0.22$  mag, while that of an M5.5 III spectral type is 0.29 mag (Bessell & Brett 1988), see compilation by Tokunaga (2000)). This gives quite a similar colour excess in both cases,  $E(H - K_S) = (H - K_S)_{\text{obs}} - (H - K_S)_0$ , of 2.12 mag and 2.05 mag for M2 I and M5 III, respectively. From the Wang & Chen (2019) near-IR extinction law the relation  $A_K = 1.33 \times E(H - K_S)$  gives  $A_K = 2.82$  mag and 2.72 mag for M2 I and M5 III, respectively. This translates to around 36 magnitudes of visual extinction using  $A_K = 0.078 A_V$ , i.e. the source is extremely reddened even though its projected location is just offset from the densest submm cores, see Fig. 7. The expected absolute magnitude of an M5 giant is  $M_V = -0.3$  mag and that of an M2 supergiant is  $M_V = -5.6$  mag (Cox 2000). The respective intrinsic colours from the above references are  $V - K = 5.96$  mag and gives  $M_K = -6.3$  mag (M5 giant) and  $V - K = 4.1$  mag giving  $M_K = -9.7$  mag (M2 supergiant). We can make a rough estimate of the distances required to reach such absolute K-band magnitudes via the relation  $M_K = m_K - A_K - 5 \log d - 5$ , and we find 1.2 kpc and 5.7 kpc for the M5 giant and the M2 supergiant, respectively. Thus, we can not use the distance argument to exclude the possibility that the source is a late M-type giant. The measured extinction requires the source to be behind the star formation region at 1.1 kpc. If it is a giant, however, the uncertainties in the above reasoning would put it at a distance compatible with the cloud, but owing to the advanced age of a giant, it would be unlikely that it is related to the cloud.

## 5. SUMMARY

1. The IRAS 00267+6511 region, located towards the outer Galaxy at a distance of 1.1 kpc, comprises embedded on-going star formation. Both millimetre (CO and CS) lines and 850 $\mu\text{m}$  continuum emission reveal the presence of dense gas and dust in a molecular cloud containing one dense clump (PGCC G120.67+2.66) resolved into five SCUBA cores.
2. Near- and mid-IR photometry is used to identify 38 YSOs with infrared excesses and/or variability, giving an average stellar surface density of 24 YSO  $\text{pc}^{-2}$  and reaching up to 113 YSO  $\text{pc}^{-2}$  in the richest populated submm core.
3. We classify 9 bona-fide Class Is and 8 bona-fide Class IIs, and most of the remaining YSOs are likely to be of Class II category. The high Class I/Class II number ratio suggests a very young age, and the spatial distribution of the YSOs with respect to the dense submm cloud cores, as well as the embeddedness, suggests that star formation is still in a very early stage.

4. Near-IR imaging reveals in one of the dense cores an hour-glass shaped nebula, likely the result of a deeply embedded YSO carving out its dust cocoon through a bipolar outflow. Another core shows signs of a protostellar jet. The third major core contains the most luminous 22  $\mu\text{m}$  embedded Class I source and could be the least evolved core.
5. We have discovered a very bright and reddened object seen towards the centre of this star formation region. Its spectrum shows it to have a cool temperature, we assume the infrared spectral type is around M2, and it is likely a red supergiant. If so, it is located far behind the cloud in the outer Galaxy and was previously unknown, despite its brightness, due to the very high foreground extinction in this region.

Part of this work was supported by Fundação para a Ciência e a Tecnologia (FCT) through the research grants UIDB/04434/2020 and UIDP/04434/2020. JLY acknowledges support from Onsala Space Observatory for the provisioning of its facilities/observational support. The Onsala Space Observatory national research infrastructure is funded through Swedish Research Council grant No 2017-00648.

Partly based on observations made with the Nordic Optical Telescope, owned in collaboration by the University of Turku and Aarhus University, and operated jointly by Aarhus University, the University of Turku and the University of Oslo, representing Denmark, Finland and Norway, the University of Iceland and Stockholm University at the Observatorio del Roque de los Muchachos, La Palma, Spain, of the Instituto de Astrofísica de Canarias.

This publication makes use of data products from the Wide-field Infrared Survey Explorer, which is a joint project of the University of California, Los Angeles, and the Jet Propulsion Laboratory/California Institute of Technology, funded by the National Aeronautics and Space Administration.

This publication makes use of data products from the Two Micron All Sky Survey, which is a joint project of the University of Massachusetts and the Infrared Processing and Analysis Center/California Institute of Technology, funded by the National Aeronautics and Space Administration and the National Science Foundation.

This research has made use of the SIMBAD database, operated at CDS, Strasbourg, France.

This research has made use of the VizieR catalogue access tool, CDS, Strasbourg, France (DOI : 10.26093/cds/vizieR). The original description of the VizieR service was published in 2000, A&AS 143, 23.

This work has made use of data from the European Space Agency (ESA) mission *Gaia* (<https://www.cosmos.esa.int/gaia>), processed by the *Gaia* Data Processing and Analysis Consortium (DPAC, <https://www.cosmos.esa.int/web/gaia/dpac/consortium>). Funding for the DPAC has been provided by national institutions, in particular the institutions participating in the *Gaia* Multilateral Agreement.

## REFERENCES

- Abbott, T. M., Aspin, C., Sorensen, A. N., et al. 2000, in Society of Photo-Optical Instrumentation Engineers (SPIE) Conference Series, Vol. 4008, Optical and IR Telescope Instrumentation and Detectors, ed. M. Iye & A. F. Moorwood, 714–719
- André, P., Di Francesco, J., Ward-Thompson, D., et al. 2014, in Protostars and Planets VI, ed. H. Beuther, R. S. Klessen, C. P. Dullemond, & T. Henning, 27–51
- Bessell, M. S. & Brett, J. M. 1988, *PASP*, 100, 1134
- Brand, J. & Blitz, L. 1993, *A&A*, 275, 67
- Comerón, F., Djupvik, A. A., Schneider, N., & Pasquali, A. 2016, *A&A*, 586, A46
- Comerón, F., Torra, J., Chiappini, C., et al. 2004, *A&A*, 425, 489
- Connelley, M. S. & Reipurth, B. 2018, *ApJ*, 861, 145
- Cox, A. N. 2000, *Allen’s astrophysical quantities*
- Cutri, R. M., Skrutskie, M. F., van Dyk, S., et al. 2003, *VizieR Online Data Catalog: 2MASS All-Sky Catalog of Point Sources (Cutri+ 2003)*, *VizieR On-line Data Catalog: II/246*. Originally published in: 2003yCat.2246...0C
- Davies, B., Figer, D. F., Kudritzki, R.-P., et al. 2007, *ApJ*, 671, 781
- Djupvik, A. A. & Andersen, J. 2010, in *Astrophysics and Space Science Proceedings*, Vol. 14, Highlights of Spanish Astrophysics V, 211
- Dunham, M. M., Allen, L. E., Evans, Neal J., I., et al. 2015, *ApJS*, 220, 11
- Eden, D. J., Liu, T., Kim, K.-T., et al. 2019, *MNRAS*, 485, 2895
- Egan, M. P., Price, S. D., Kraemer, K. E., et al. 2003, *VizieR Online Data Catalog: MSX6C Infrared Point Source Catalog. The Midcourse Space Experiment Point Source Catalog Version 2.3 (October 2003)*, *VizieR On-line Data Catalog: V/114*. Originally published in: Air Force Research Laboratory Technical Report AFRL-VS-TR-2003-1589 (2003)
- Egan, M. P., Price, S. D., Moshir, M. M., Cohen, M., & Tedesco, E. 1999, *The Midcourse Space Experiment Point Source Catalog Version 1.2 Explanatory Guide*, Technical Report, AD-A381933; AFRL-VS-TR-1999-1522
- Elias, J. H., Frogel, J. A., & Humphreys, R. M. 1985, *ApJS*, 57, 91
- Evans, Neal J., I., Dunham, M. M., Jørgensen, J. K., et al. 2009, *ApJS*, 181, 321
- Foster, J. B., Cottaar, M., Covey, K. R., et al. 2015, *ApJ*, 799, 136
- Frerking, M. A., Langer, W. D., & Wilson, R. W. 1982, *ApJ*, 262, 590
- Gaia Collaboration, Prusti, T., de Bruijne, J. H. J., et al. 2016, *A&A*, 595, A1
- Gaia Collaboration, Vallenari, A., Brown, A. G. A., et al. 2023, *A&A*, 674, A1
- Greene, T. P., Wilking, B. A., Andre, P., Young, E. T., & Lada, C. J. 1994, *ApJ*, 434, 614
- Guo, H.-L., Chen, B.-Q., Li, G.-X., et al. 2020, *Monthly Notices of the Royal Astronomical Society*, 500, 3743
- Gutermuth, R. A., Megeath, S. T., Myers, P. C., et al. 2009, *ApJS*, 184, 18
- Gutermuth, R. A., Megeath, S. T., Pipher, J. L., et al. 2005, *ApJ*, 632, 397
- Harvey, P., Merín, B., Huard, T. L., et al. 2007, *ApJ*, 663, 1149
- Kaas, A. A. 1999, *AJ*, 118, 558
- Koenig, X. P. & Leisawitz, D. T. 2014, *ApJ*, 791, 131
- Lada, C. J. & Lada, E. A. 2003, *ARA&A*, 41, 57
- Lada, C. J. & Wilking, B. A. 1984, *ApJ*, 287, 610
- Lançon, A. & Wood, P. R. 2000, *A&AS*, 146, 217
- Levesque, E. M., Massey, P., Olsen, K. A. G., et al. 2005, *ApJ*, 628, 973
- May, J., Alvarez, H., & Bronfman, L. 1997, *A&A*, 327, 325
- McCaughrean, M. J., Rayner, J. T., & Zinnecker, H. 1994, *ApJ*, 436, L189
- Palmeirim, P. M. & Yun, J. L. 2010, *A&A*, 510, A51
- Planck Collaboration, Adam, R., Ade, P. A. R., et al. 2016, *A&A*, 594, A1
- Planck Collaboration, Ade, P. A. R., Aghanim, N., et al. 2011, *A&A*, 536, A7
- Reid, M. J., Menten, K. M., Brunthaler, A., et al. 2019, *ApJ*, 885, 131
- Reid, M. J., Menten, K. M., Brunthaler, A., et al. 2014, *ApJ*, 783, 130
- Skrutskie, M. F., Cutri, R. M., Stiening, R., et al. 2006, *AJ*, 131, 1163
- Sofue, Y. 2011, *PASJ*, 63, 813
- Stead, J. J. & Hoare, M. G. 2009, *MNRAS*, 400, 731
- Strom, K. M., Strom, S. E., & Merrill, K. M. 1993, *ApJ*, 412, 233
- Szegedi-Elek, E., Ábrahám, P., Wyrzykowski, Ł., et al. 2020, *ApJ*, 899, 130
- Tobin, J. J. & Sheehan, P. D. 2024, *arXiv e-prints*, arXiv:2403.15550
- Tokunaga, A. T. 2000, in *Allen’s Astrophysical Quantities*, ed. A. N. Cox, 143
- Wallace, L. & Hinkle, K. 1997, *ApJS*, 111, 445
- Wang, S. & Chen, X. 2019, *ApJ*, 877, 116
- Wenger, T. V., Balsaer, D. S., Anderson, L. D., & Bania, T. M. 2018, *ApJ*, 856, 52
- Winston, E., Hora, J. L., & Tolls, V. 2020, *AJ*, 160, 68
- Wright, E. L., Eisenhardt, P. R. M., Mainzer, A. K., et al. 2010, *AJ*, 140, 1868
- Yuan, J., Wu, Y., Liu, T., et al. 2016, *ApJ*, 820, 37
- Yun, J. L., Clemens, D. P., Moreira, M. C., & Santos, N. C. 1997, *ApJ*, 479, L71
- Yun, J. L., Elia, D., Djupvik, A. A., Torrelles, J. M., & Molinari, S. 2015, *MNRAS*, 452, 1523
- Yun, J. L., Santos, C. A., Clemens, D. P., et al. 2001, *A&A*, 372, L33
- Zhang, C.-P., Liu, T., Yuan, J., et al. 2018, *The Astrophysical Journal Supplement Series*, 236, 49
- Zhang, T., Wu, Y., Liu, T., & Meng, F. 2016, *ApJS*, 224, 43

This paper was built using the Open Journal of Astrophysics L<sup>A</sup>T<sub>E</sub>X template. The OJA is a journal which

provides fast and easy peer review for new papers in the **astro-ph** section of the arXiv, making the reviewing process simpler for authors and referees alike. Learn more at <http://astro.theoj.org>.

TABLE 3  
THE 17 YSOs FOUND FROM WISE MID-IR COLOURS, LISTED TOGETHER WITH 2MASS NEAR-IR COLOURS AND ERRORS WHEN AVAILABLE. THE YSO CLASS IS GIVEN IN THE LAST COLUMN. SEE SECT. 3.1 FOR DETAILS.

WISE ID	J - H mag	$\sigma_{E-J}$ mag	H - K <sub>S</sub> mag	$\sigma_{H-K_S}$ mag	[3.4] - [4.6] mag	$\sigma_{3.4-4.6}$ mag	[4.6] - [12] mag	$\sigma_{4.6-12}$ mag	[4.6] mag	$\sigma_{4.6}$ mag	Class
J002941.83+652631.9	1.16	0.09	0.78	0.07	1.23	0.03	2.67	0.05	11.60	0.02	I <sup>a</sup>
J002954.81+652659.2					1.92	0.08	3.72	0.04	12.26	0.03	I
J002952.30+652725.3	2.44		1.44	0.06	0.88	0.03	3.29	0.03	11.39	0.02	I
J002950.58+652719.6	2.01	0.15	2.30	0.08	1.89	0.03	2.90	0.02	8.42	0.02	I
J002932.58+652510.0					2.81	0.03	3.76	0.02	9.16	0.02	I
J002929.28+652746.0	2.57		1.84		2.56	0.03	3.51	0.02	8.33	0.02	I
J002931.45+652718.4	1.67		1.82	0.10	1.40	0.03	2.81	0.02	8.75	0.02	I
J002937.06+652813.1	1.88		1.71		1.62	0.03	2.12	0.02	8.18	0.02	I <sup>b</sup>
J002940.09+652811.1	1.06	0.12	0.94	0.09	1.27	0.03	2.62	0.03	10.73	0.02	I
J002949.31+652528.5	1.93		1.11	0.05	0.76	0.03	1.86	0.03	9.65	0.02	II
J002952.88+652539.9	1.65		1.41	0.10	0.96	0.03	1.94	0.05	11.63	0.02	II
J002951.92+652702.7	1.27	0.07	0.57	0.06	0.79	0.03	2.32	0.05	11.74	0.02	II
J002932.47+652637.7	0.91	0.04	0.56	0.04	0.65	0.03	1.80	0.03	9.07	0.02	II
J002925.19+652637.7	1.08	0.06	0.81	0.05	0.70	0.03	1.72	0.06	11.57	0.02	II
J002928.25+652634.1	1.31	0.05	0.70	0.05	0.57	0.04	2.00	0.05	11.39	0.02	II
J002937.69+652621.7	1.15	0.05	0.76	0.05	0.84	0.03	2.42	0.03	10.66	0.02	II
J002941.52+652730.9	1.97		1.29		1.04	0.03	1.69	0.03	9.41	0.02	II

**Notes:**

<sup>a</sup>Has a deviating proper motion and is located outside the dense cores.

<sup>b</sup>Candidate WISE originating source for the hour-glass shaped nebula, in which case both coordinates and 2MASS cross-correlation, here taken from the WISE catalogue, are uncertain, See Sect. 4.3.

TABLE 4  
THE 21 ADDITIONAL YSO CANDIDATES FOUND IN THE NOTCAM AND 2MASS SAMPLE, SELECTED FROM EITHER NEAR-IR EXCESS OR VARIABILITY OR BOTH. THE CROSS-CORRELATED 2MASS POINT SOURCE DETECTION IS GIVEN AS AN ID WHILE THE RA/DEC COORDINATES, AS WELL AS THE NEAR-IR MAGNITUDES AND COLOURS ARE FROM THE NOTCAM DATA.

2MASS-ID	RAJ2000 deg	DEJ2000 deg	H mag	$\sigma_H$ mag	J - H mag	$\sigma_{J-H}$ mag	H - K <sub>S</sub> mag	$\sigma_{H-K}$ mag	YSO criterion
00292061+6528458	7.33595	65.47936	15.85	0.03	1.18	0.05	0.915	0.16	NIR excess
00292316+6526123	7.34653	65.43672	14.83	0.03	1.22	0.04	0.576	0.10	Variable H
00292601+6526014	7.35837	65.43375	12.12	0.03	0.54	0.03	0.432	0.06	NIR excess
00292700+6526051	7.36250	65.43478	14.53	0.03	1.03	0.04	0.610	0.09	NIR excess
00292916+6526190	7.37149	65.43862	14.23	0.03	0.76	0.04	0.549	0.08	NIR excess
00292956+6526017	7.37326	65.43379	15.19	0.03	1.59	0.04	0.856	0.10	Variable H
00293083+6526490	7.37846	65.44699	12.72	0.03	2.31	0.04	1.301	0.06	NIR excess
00293280+6527210	7.38667	65.45583	15.25	0.03	2.26	0.05	1.021	0.10	Variable K <sub>S</sub>
	7.38748	65.47388	18.80	0.06	0.73	0.08	0.696	0.09	NIR excess
00293391+6527157	7.39133	65.45448	16.59	0.04	2.66	0.08	1.802	0.06	NIR excess
	7.39428	65.46428	16.55	0.04	1.46	0.06	0.996	0.06	NIR excess
00293683+6528128	7.40348	65.47021	15.91	0.04	2.82	0.09	1.947	0.10	NIR excess
00293773+6528134	7.40753	65.47038	15.37	0.04	1.96	0.06	1.320	0.06	NIR excess
00293889+6528160	7.41210	65.47108	17.05	0.04	2.01	0.07	1.498	0.06	NIR excess
00293975+6525030	7.41569	65.41750	14.82	0.03	0.81	0.04	0.032	0.15	Variable J + K <sub>S</sub>
	7.41967	65.46547	18.58	0.05	0.63	0.07	0.511	0.09	NIR excess
00294167+6527049	7.42367	65.45137	14.61	0.03	1.23	0.04	0.231	0.11	Variable H + K <sub>S</sub>
00294396+6526034	7.43321	65.43431	13.95	0.03	0.97	0.04	0.601	0.08	NIR excess, bipolar H <sub>2</sub> jet
00294693+6528014	7.44546	65.46706	14.58	0.03	1.03	0.04	-0.176	0.13	Variable K <sub>S</sub>
00294889+6525251	7.45369	65.42361	15.88	0.03	2.11	0.06	1.322	0.12	NIR excess, Variable H + K <sub>S</sub>
00295286+6526412	7.47025	65.44478	13.43	0.03	1.96	0.04	0.804	0.07	Variable K <sub>S</sub>